Physics in Medicine & Biology

High-resolution time-of-flight PET detector with 100 ps coincidence time resolution using a side-coupled phoswich configuration

To cite this article before publication: Min Sun Lee *et al* 2021 *Phys. Med. Biol.* in press https://doi.org/10.1088/1361-6560/ac01b5

High-resolution time-of-flight PET detector with 100 ps coincidence time resolution using a side-coupled phoswich configuration

Min Sun Lee[1,6], Joshua W. Cates[2], Andrea Gonzalez-Montoro[1], and Craig S. Levin[1,3,4,5]

[1]Department of Radiology, Molecular Imaging Program at Stanford, School of Medicine, Stanford University, California, United States.

[2]Applied Nuclear Physics Program, Lawrence Berkeley National Laboratory, California, United States.

[3]Department of Physics, Stanford University, California, United States

[4]Department of Electrical Engineering, Stanford University, California, United States.

[5]Department of Bioengineering, Stanford University, California, United States.

[6]Nuclear Emergency & Environmental Protection Division, Korea Atomic Energy Research Institute, Daejeon, Republic of Korea

Name and address for correspondence and reprint requests:

Craig S. Levin, PhD

James H. Clark Center, 318 Campus Drive, E 1.1, Stanford, CA 94305-5427, United States

Email: cslevin@stanford.edu

Phone: +1-650-736-7211

Short title: Side-coupled phoswich PET detector

Keywords: **high resolution, time-of-flight, 100 ps, coincidence time resolution, phoswich, silicon photomultipliers, positron emission tomography**

ABSTRACT

Photon time-of-flight (TOF) capability in positron emission tomography (PET) enables reconstructed image signal-to-noise ratio (SNR) improvement. With the coincidence time resolution (CTR) of 100 picosecond (ps), a 5-fold SNR improvement can be achieved with a 40 cm diameter imaging subject, relative to a system without TOF capability. This 100 ps CTR can be achieved for a *clinically relevant* detector design (crystal element length ≥20 mm with reasonably high crystal packing fraction) using a side-readout PET detector configuration that enables 511 keV photon interaction depth-independent light collection efficiency (LCE) and lower variance in scintillation photon transit time to the silicon photomultiplier (SiPM). In this study, we propose a new concept of TOF-PET detector to achieve high (<2 mm) resolution, using a "side-coupled phoswich" configuration, where two crystals with different decay times (τ_d) are coupled in a side-readout configuration to a common row of photosensors. The proposed design was validated and optimized with GATE Monte Carlo simulation studies to determine an efficient detector design. Based on the simulation results, a proof-of-concept side-coupled phoswich detector design was developed comprising two LSO crystals with the size of 1.9×1.9×10 mm^3 with decay times of 34.39 and 43.07 ns, respectively. The phoswich crystals were side-coupled to the same three 4×4 mm^2 SiPMs and detector performances were evaluated. As a result of the experimental evaluation, the side-coupled phoswich configuration achieved CTR of 107±3 ps, energy resolution of 10.5±1.21% at 511 keV and >95% accuracy in identifying interactions in the two adjacent 1.9×1.9×10 mm^3 crystal elements using the time-over-threshold (ToT) technique. Based on our results, we can achieve excellent spatial and energy resolution in addition to ~100 ps CTR with this novel detector design.

1. INTRODUCTION

By measuring the arrival times of the 511 keV annihilation photons with high precision, time-of-flight (TOF) information is used to constrain the photon emission point along every line-of-response (LOR), thus enhancing reconstructed image signal-to-noise ratio (SNR) (Jacoby *et al* 2011, Surti and Karp 2016, Conti and Bendriem 2019). State-of-the-art commercial TOF-PET systems have achieved photon pair coincidence time resolution (CTR) performance as low as 214 picoseconds (ps) full-width at half maximum (FWHM), which can constrain events to a 3.2 cm segment along LORs (Siemens Biograph Vision Technical Sheet 2019). Recently, with the innovations in scintillation crystal, photosensor, and electronic readout technologies, sub-100 ps FWHM CTR for ≥20 mm length scintillation crystal elements and good crystal packing fraction needed in a clinical PET system is now achievable at the detector-level (Cates and Levin 2018). Others have also achieved sub-100 ps CTR with $2 \times 2 \times 20$ mm^3 crystals coupled end-on to the center of 4×4 mm^2 SiPMs (Gundacker *et al* 2019). With 100 ps FWHM CTR, one could narrow down the TOF constraint during the back-projection process to 1.5 cm, enabling a 5-fold reconstructed image SNR improvement relative to a system with non-TOF capability for a 40 cm diameter imaging subject. The 5-fold SNR improvement allows reduced scanning times with the same radiotracer dose or may allow significant dose reduction to the patients with the same scanning time, thus paving a way for broadening the use of PET scanning (Surti 2015).

In addition to the reconstructed image SNR improvement using 100 ps CTR TOF information, there are other technical benefits such as improved contrast-to-noise ratio resulting in improved lesion detectability, fast convergence for reconstruction algorithms to estimate PET emission data and attenuation maps for PET/MR application (Mollet *et al* 2012), and more accurate scatter corrections, which are routine needs in quantitative PET imaging (Conti 2011).

Besides the rapid improvement in CTR performance, current state-of-the-art clinical TOF-PET systems are able to provide 3-4 mm reconstructed image spatial resolution at the system center (Hsu *et al* 2017, Miller *et al* 2015, Sluis *et al* 2019, Siemens Biograph Vision Technical Sheet 2019), and state-of-the-art brain-dedicated PET designs are able to provide 2-3 mm spatial resolution across the FOV (Yamaya *et al* 2008, Abraham and Feng 2011, Tashima *et al* 2016). In addition to improving image SNR, enhancing spatial resolution is also desirable and necessary for some applications such as neurological imaging or detection of small-size lesions and organs. Common approaches to improve the spatial resolution includes using smaller or multi-layers of crystals and sensors (Shao *et al* 2002, Inadama *et al* 2006, Watanabe *et al* 2017) or using approaches based on light sharing (Miyaoka *et al* 2009, Ito *et al* 2013). However, these approaches usually compromise the CTR performances due to the reduced LCE and time walk caused by the varying depth-of-interaction (DOI) blur (Loignon-Houle *et al* 2020). Moreover, in those high-resolution applications, TOF capability did not play a significant role due to their smaller bore size than that of whole-body scanners. However, at the level of 100 ps CTR performance, which provides LOR constraints of 1.5 cm during the image reconstruction process, TOF capabilities will further enhance image SNR in small diameter systems as well.

Recently, several groups proposed new approaches to achieve high spatial resolution and good CTR of sub-200 ps at the same time. Pizzichemi *et al* 2019 proposed using light sharing techniques at the radiation receiving end and reported 157 ps CTR and 3 mm DOI resolution using 1.53×1.53×15 mm^3 LYSO crystals coupled to SiPM arrays. Kang *et al* 2020 reported 188 ps CTR and 2.9 mm DOI resolution using a single saw-cut 2.9×2.9×20 mm^3 LYSO crystals in dual-ended readout configuration with air coupling between crystal and reflector. Moreover, machine learning algorithms have been also proposed as an option to achieve excellent CTR. Borghi *et al* 2016 achieved 147 ps CTR and ~ 1.1 mm spatial resolution using maximum likelihood interaction time estimation method in a dual-ended readout monolithic PET detector

with a 32×32×22 mm^3 LYSO:Ce crystal. La Bella *et al* 2020 proposed convolutional neural network based algorithm to improve CTR. They performed a simulation study of a detector module consisted of 1.5×1.5×20 mm^3 LYSO crystals and prismatoid light guide arrays, reporting < 2 mm spatial resolutions and an improvement of more than 50% in CTR when including both DOI information and multiple timestamps. However, so far, there is no such group who has achieved CTR performance of sub-100 ps or near-100 ps CTR while maintaining 2 mm spatial resolution and DOI resolution at the same time.

Hence, in this work, we suggest a new concept for a high-resolution PET detector design that can achieve 100 ps CTR, the side-coupled phoswich detector. To achieve 100-ps CTR, we used the side-readout approach of coupling the scintillation crystal to multiple photosensors on their long side (Levin 2002, Cates and Levin 2018). This side-readout concept has some benefits in comparison to the standard end-readout approach of coupling the crystal to the photosensor by its end. The side-readout design allows nearly complete light collection with lower photon transit time jitter, and its excellent CTR performance has been validated through previous studies (Cates and Levin 2015, Cates and Levin 2018). Moreover, the side-readout configuration yields intrinsic DOI information (related to the SiPM pixel size). However, this side-readout design is limited in terms of high-resolution applications, because reducing the size of SiPM pixels along with the crystal element size is technically challenging and costly. To achieve high-resolution, we suggest a novel configuration that employs a phoswich approach (e.g. see Holte *et al* 1987) in combination with the side-readout configuration approach. The proposed design was validated and optimized with GATE Monte Carlo simulation studies to determine an efficient detector design. Then a proof-of-concept detector design was developed based on the simulation results and the detector performances was experimentally evaluated.

2. MATERIALS AND METHODS

2.1 Side-coupled phoswich detector

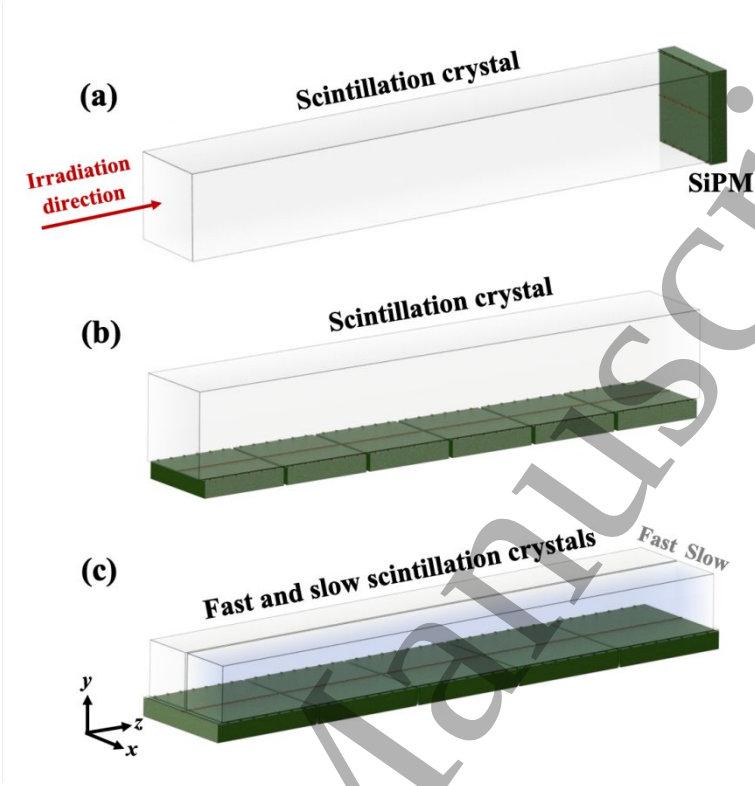

Figure 1 (a) Conventional *end-readout* design comprises a single scintillation crystal element (e.g. $3 \times 3 \times 20$ mm^3) coupled end-on to the photodetector, in this case to a single SiPM (e.g. 3×3 mm^2). (b) *Side-readout* configuration where a single scintillation crystal element (e.g. $3 \times 3 \times 20$ mm^3) is side-coupled to an array of SiPMs (e.g. 3×3 mm^2) (Cates and Levin 2018]. (c) Proposed *side-coupled phoswich* design where one fast (white) and one slow (light-blue) scintillation crystals (e.g. $1.9 \times 1.9 \times 20$ mm^3 in this paper) are both side-coupled to the same 1×5 linear array of SiPMs (e.g. 4×4 mm^2).

A detector with good CTR performance requires bright and fast scintillation crystals, high light collection efficiency (LCE) and low scintillation light transit time from the point of interaction within the crystal to the photosensor, a photosensor with very low single photon time resolution (SPTR), and fast analog front-end electronics with low noise. To meet these requirements, we employed the side-readout configuration in this study, where a long side face

of a scintillation crystal is coupled to the same array of SiPMs. Compared to the conventional end-readout configuration (Figure 1(a)), the side-readout configuration (Figure 1(b)) allows for nearly complete LCE (Levin 2002) for crystals with higher aspect ratio and reduced scintillation light transit distance and variance (Yeom *et al* 2014, Cates *et al* 2015, Cates *et al* 2018). Consequently, the side-readout configuration provides higher LCE with lower photon transit time jitter that leads to better CTR performance compared to the conventional end-readout configuration. In a previous study, we experimentally proved that the side-readout approach achieves CTR performance of 102 ps when using 3×3×20 mm^3 LGSO crystals side-coupled to 3×3 mm^2 SiPMs, while the end-readout for the same crystals and SiPMs showed a CTR of 137 ps (Cates and Levin 2018).

However, this side-readout design is limited in terms of high-resolution applications, because reducing the size of SiPM pixels along with the crystal element size is technically challenging and costly. Moreover, as the size of the SiPM pixel gets smaller, the number of microcells within the SiPM pixel decreases leading to energy non-linearity of the detector (Regazzoni *et al* 2017). This energy non-linearity will be more significant in the side-readout configuration, where most of the photons are collected in SiPMs. Also, an array comprising smaller SiPM pixels has larger overall dead area, resulting in lower packing fraction and thus lower 511 keV photon detection sensitivity (Almeida *et al* 2008). Therefore, we suggest a side-coupled phoswich configuration as a solution to improve the spatial resolution in the side-readout configuration, while maintaining excellent CTR. As shown in Figure 1(c), two scintillation crystals with different decay times (τ_d) were placed adjacent to each other and side-coupled to the same array of SiPMs. By employing two smaller crystals instead of one larger crystal coupled to the same SiPMs, we can achieve better spatial resolution in a phoswich scheme if the two crystal elements have sufficiently different decay time. The proposed side-coupled phoswich configuration allows us to reduce the number of photodetectors (or number

of readout channels) since it can use larger area SiPMs. However, slight degradation in timing performance is expected due to higher capacitance of larger SiPM areas and slower decay time of one of the elements. By using this side-coupled phoswich configuration, we achieved good spatial resolution while still maintaining excellent CTR performance.

2.2 Monte Carlo simulation study

In order to investigate the proposed concept design and to find appropriate design parameters, a Monte Carlo simulation study was conducted using GATE v.8.0 toolkit (Jan *et al* 2004, Jan *et al* 2011) with optical photon tracking. For simulating photon interactions at crystal surfaces and medium boundaries, we used the "ground model" based on the UNIFIED model. A ground surfaces in GATE simulation is composed of very small micro-facets relative to average surface normal (Levin and Moisan 1996). The simulated side-coupled phoswich configuration consisted of two LSO crystals (Lu_2SiO_5; effective Z=66, ρ=7.4g/cm^3; light yield=30,000 photons/MeV, refractive index=1.82) coupled to arrays of SiPM pixels (Si; ρ=2.33g/cm^3). The properties of the simulated LSO crystals were obtained from literature (LSO ΣTech^{UK} datasheet). Mimicking the crystals used later in the experimental set-up, two LSO crystals were simulated with different decay times (τ_d) of 34.39 and 43.07 ns and the chemically etched surfaces were simulated with the sigma-alpha (σ_α, defines the standard deviation of the Gaussian distribution of micro-facets around the average surface normal) of 3.8 (Janecek *et al* 2010). All the photon interactions at the crystal surface were set to follow specular reflection based on the microfacet orientations; *specularlobeconstant* parameter in GATE was set to be 1. The outer faces of crystals were wrapped with the 65 μm thick ESR reflector and all optical interfaces except the readout face were set to have the surface finish of *groundbackpainted* assuming Lambertian reflection (van der Laan *et al* 2010) with the reflectivity of 0.98. The

simulated SiPM pixel had dimensions of 4×4×0.379 mm^3 with an active area of 3.93×3.93 mm^2 that corresponds to the real SiPM geometry of the 4×4 mm^2 MicroFJ-40035 SiPMs used in experiments (ON Semiconductor 2018). We tested different phoswich configurations with different crystal element dimensions of 1.9×1.9×10, 1.9×1.9 ×20, and 1.9×3.0×20 mm^3, respectively. For 1.9×1.9×10 mm^3 phoswich crystals, different gap material within 0.1 mm gap between the two adjacent phoswich crystals was considered to be filled with air, optical grease ($C_1H_1O_1$; ρ=1.0 g/cm^3; refractive index 1.465), 65 μm thick ESR with air gap, and ESR reflector with optical grease. Photons generated within the crystals travels through each simulated detector configuration; once photons were detected in the SiPM pixels, each event was recorded as an output. The EM standard package of GATE, including the scintillation process, optical tracking process including absorption, and boundary and Rayleigh scattering was used for the physics list in GATE. We have not included Cerenkov effect in this study. A pair of detectors were uniformly irradiated with a back-to-back annihilation point source with 511-keV energy and time-series scintillation photons were recorded. Moreover, as a comparison, the original side-readout configuration was simulated where a single polished LSO crystal (Lu_2SiO_5; ρ=7.4g/cm^3; light yield=30,000 photons/MeV, τ_d=34.39 ns) with dimensions of 3×3×10 and 3×3×20 mm^3 were coupled to a linear array of 3×3 mm^2 SiPMs. Surfaces of single side-readout crystal elements were simulated to have polished surfaces with σ_α of 1.3 and *specularlobeconstant* of 1 for the relevance to the previous study (Cates and Levin 2018). All the simulated detector configurations are summarized in Table 1.

Table 1. The specifications of detector configurations and the simulation parameters used in the simulation study.

	Side-coupled phoswich detector			**Original side-readout detector (reference)**	
Crystal element dimensions [mm³]	1.9 × 1.9 × 10	1.9 × 1.9 × 20	1.9 × 3.0 × 20	3.0 × 3.0 × 10	3.0 × 3.0 × 20
Gap material between phoswich crystals	Airgap Grease Reflector + airgap Reflector + grease	Airgap		N/A	
Decay time [ns]	34.39 (fast) and 43.07 (slow)			34.39	
SiPM area [mm²]	4 × 4			3 × 3	
Surface treatment	Chemically etched (σ_α=3.8)			Polished (σ_α=1.3)	
Density [g/cm³]	7.4				
Refractive index	1.82				

To generate realistic SiPM output pulses, time-series scintillation photons distribution from GATE, were post-processed to incorporate characteristics of the SiPM and noise sources. The photon detection efficiency (PDE) of 50% (ON Semiconductor 2018) was considered in the photon distribution and single photon time resolution (SPTR) blur of 123 ps (Nemallapudi *et al* 2016) was considered in the timestamps to include the transit time spread of the SiPM (Acerbi and Gundacker 2019). The SiPM noise characteristics sources including a dark count rate of 150 kHz/mm² following a random process ($noise_{DC}(t,n)$) and measured optical crosstalk probability following a Poisson distribution ($noise_{OC}(t,n)$) were incorporated. The post-processed photon distributions were convolved with the SiPM single cell response to generate SiPM signals. Depending on the crystal size, different SiPM single cell responses (e.g. 4 × 4 mm² SiPM for phoswich crystals and 3 × 3 mm² SiPM for original side-readout detector) were incorporated. Finally, the measured analog electronic root mean square of 250 μV noise contributions were superimposed on the simulated SiPM signal. All the measured SiPM characteristics were experimentally measured at 32 V bias voltage. Every process was

simulated by a random number generator using MATLAB and summarized as a flow chart in the Figure 2.

The leading-edge discrimination (LED) method was applied on rising edge of the post-processed scintillation pulse for timestamp pickoff and LED thresholds were swept from the levels of single photon to few photons to find the optimum value. About 1,500 coincident events that fell within full-width at tenth maximum (FWTM) of the 511-keV photopeak (equivalent to energy window of 450 – 650 keV) were analyzed for 5 trials and averaged for reporting CTR values.

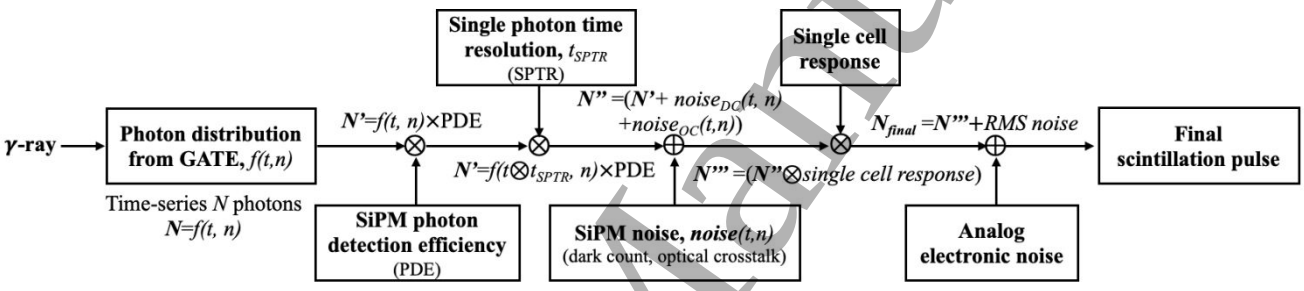

Figure 2 A flow chart showing annihilation photon event post-processing to generate a scintillation pulse in an SiPM-based readout system.

2.3 Proof-of-concept side-coupled phoswich detector

2.3.1 Crystal characterization

Two 1.9×1.9×10 mm^3 LSO crystal elements (Siemens Healthineers, Tennessee, USA) with fast and slow decay times were each tested and characterized before building the proof-of-concept phoswich detector. All the crystal samples had a chemically etched surface treatment. Rise time, decay time, and energy resolution was measured using a Hamamatsu R9779 photomultiplier tube (PMT) in side-coupled configuration as shown in Figure 3. Crystal

surfaces were wrapped using Teflon tape and optically coupled to the PMT using optical grease (BC-640, Saint Gobain, France). PMT signal was directly sent to a digital oscilloscope (DSO940, 2GHz, 20GSa/sec, Agilent, USA) for the waveform sampling. Decay time was measured by exponentially fitting the tail of waveforms within the range from 90% to 10% of the maximum pulse height; rise time was measured by exponentially fitting the rising edge of waveforms within the range from 10% to 90% of the maximum pulse height. A total of 3,500 events were used for detector performance evaluation that fell within the FWTM of 511-keV photopeak. Measurements were conducted for eight different samples of each fast and slow crystal.

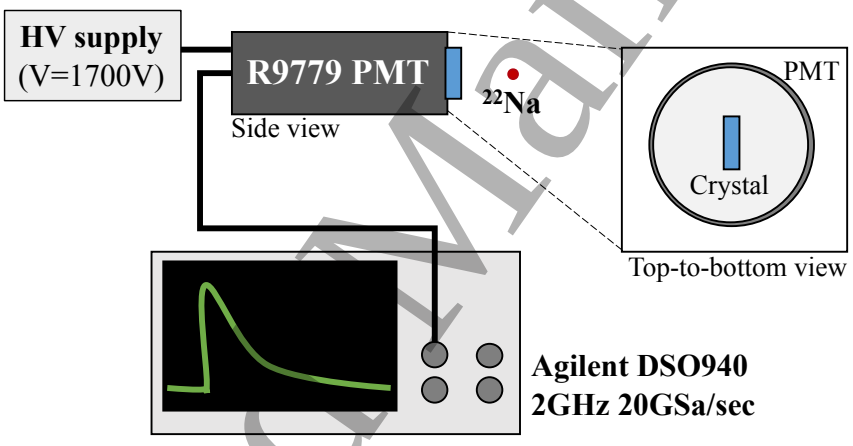

Figure 3 Measurement setup for scintillation crystal characterization using PMT.

2.3.2 Detector evaluation

To build a proof-of-concept side-coupled phoswich detector, only two 1.9×1.9×10 mm^3 LSO crystal elements were considered (Figure 4(a)), since based on simulation results, we determined 1.9×1.9×10 mm^3 crystals to be the most efficient proof-of-concept configuration, see Section 3.1. The crystals present fast and slow decay times of 34.39 ns and 43.07 ns and were side-coupled to a 5×1 array of 4×4 mm^2 SiPMs (MicroFJ-40035, OnSemi, Ireland), see

Figure 4(b) and (c). The upper three SiPMs were used to readout scintillation light from the crystals 10 mm-length side and the crystals were aligned to the top-edge of the SiPM array. A ^{22}Na point source was placed between a pair of these phoswich detectors separated by 3 cm to conduct the coincidence measurement (Figure 5(a)). Four different detector combinations were tested: 1) single fast crystal elements, 2) single slow crystal elements, 3) side-coupled phoswich crystals with air gap between adjacent crystals, and 4) side-coupled phoswich crystals with enhanced specular reflector (ESR, 3M, USA) between adjacent crystals (air-reflector-air). All the crystal outer surfaces, except for the one that is coupled to the SiPMs, were wrapped with Teflon tape.

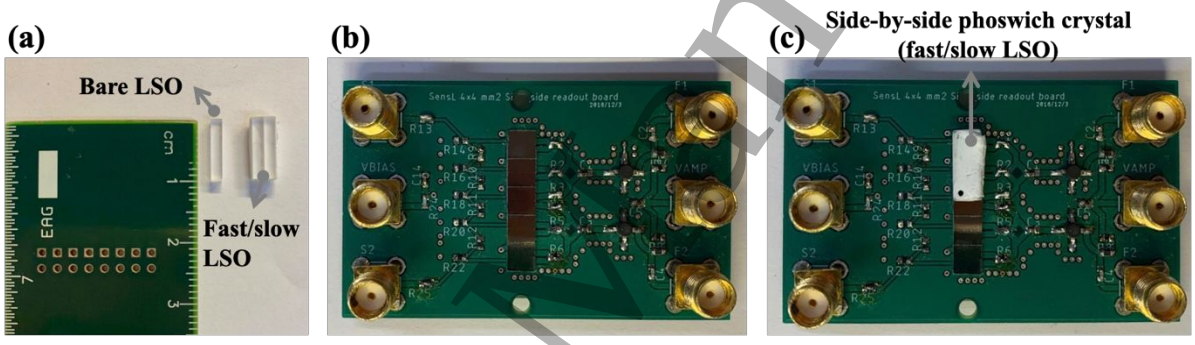

Figure 4 (a) Bare 1.9×1.9×10 mm^3 LSO scintillator crystal (left) and phoswich arrangement with fast and slow LSO crystals (right) wrapped with Teflon tape. (b) 5×1 array of 4×4 mm^2 SiPMs (c) Proposed side-coupled phoswich detector design arrangement. The black dot in the scintillator pair indicates where the fast crystal was positioned.

The 'standard outputs' (anode) of the three SiPMs coupled to the scintillators were connected and used as the energy signal and the 'fast outputs' of three SiPMs were connected to a high-bandwidth monolithic RF amplifier (MAR-6+, Minicircuits, USA) and used as the timing signal as shown in the schematic in Figure 5(b). The summed energy signal was split into two signal lines. One of the energy channel lines was sent to a time-over-threshold (ToT) board (Grant and Levin 2014). Our group has previously shown that the ToT approach better

distinguishes which element an interaction occurs in the phoswich crystal configuration compared to the conventional pulse shape discrimination method which requires an additional ADC with different integration time (Chang *et al* 2016); hence, in this study, we used the ToT values for the phoswich crystal of interaction separation. The ToT thresholds were chosen after testing several thresholds from 20 to 70% of maximum pulse height. To evaluate crystal separation performance for the phoswich crystals, crystal separation accuracy was calculated based on the acquired ToT histogram with the following equation:

$$\text{Crystal separation accuracy} = 1 - \frac{overlapping\ area}{Total\ area\ under\ curve}$$

The other split energy channel signal line was directly fed into the scope and used as a reference energy value by integrating the scintillation waveform. Moreover, SiPM energy non-linearity (saturation) correction was applied. Six photon energies from four radionuclides -^{133}Ba (80.99 keV, 356.02 keV), ^{57}Co (122 keV), ^{22}Na (511 keV, 1275 keV), and ^{137}Cs (662 keV)- were used, and the SiPM photopeak values were plotted with the real energy value and fitted with a polynomial function. The fitted SiPM response was then corrected to a linear function assuming an SiPM linear energy response.

The amplified timing signal was directly fed into the digital oscilloscope and the LED method was applied on the digitized waveform for timing pickoff. LED thresholds were tested from 0.6 mV to 7.0 mV with 0.2 mV step size. Due to the natural time-walk characteristics of the LED method, time-walks occurring in different coincidence pairs of fast-fast, slow-slow, fast-slow, and slow-fast crystals may lead to worse CTR performance. Hence, a time-walk correction was applied on the time difference histogram by correcting the timing offsets in each coincidence pair. The SiPM bias voltage was tested from 28 V to 32 V while the typical breakdown voltage of MicroFJ-40035 was 24.5 V provided by the vendor datasheet (ON Semiconductor 2018). For the performance evaluation, a total of 3,500 events were used that

fell within FWTM of 511-keV photopeak, and the measurement was repeated eight times for each combination.

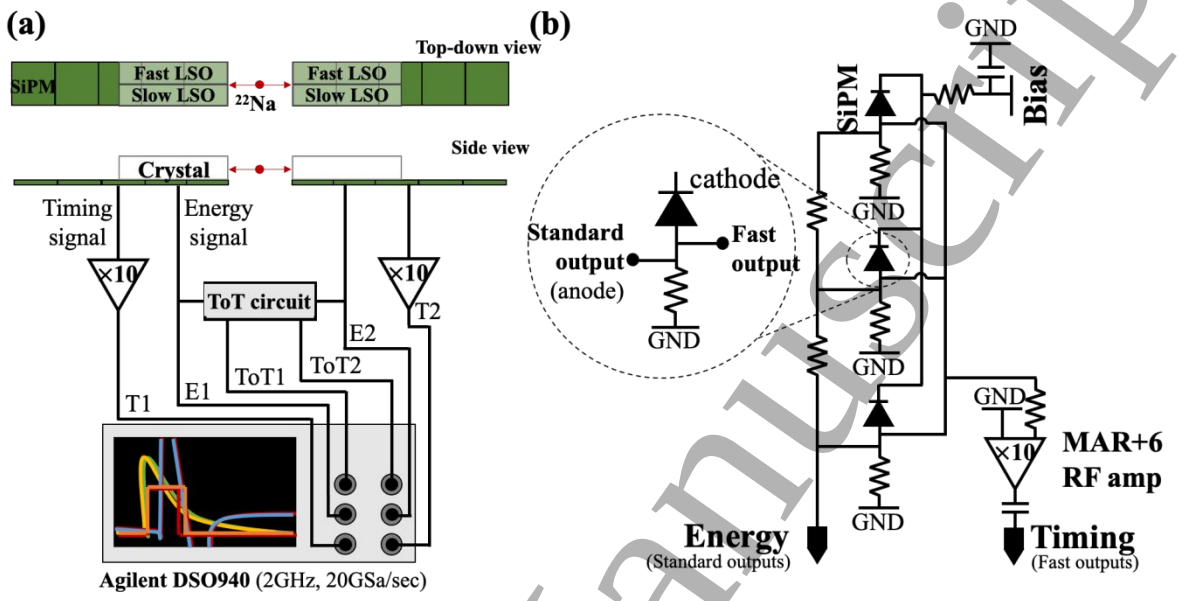

Figure 5 (a) Coincidence measurement setup for side-coupled phoswich detector that consisted of a pair of side-coupled phoswich crystals (1.9x1.9 mm^2 cross section) coupled to a linear array of 4x4 mm^2 SiPMs. (b) Schematic for the side-coupled phoswich detector front-end readout scheme.

3. RESULTS

3.1 Simulation results

From the simulation studies, we achieved an excellent CTR of 104±1 ps with 1.9×1.9×10 mm^3 phoswich crystals side-coupled to three 4×4 mm^2 SiPMs with an airgap between the crystals (see Figure 6(a)). With longer and larger crystal element, worse CTR performance of 113±1 ps and 117±1 ps CTR was observed for 1.9×1.9×20 mm^3 and 1.9×3×20 mm^3 phoswich crystals, respectively. The original side-readout configuration, which corresponds to the experimental results in our previous studies (e.g. Cates and Levin 2018), where the single fast crystal was side-coupled to an array of 3×3 mm^2 SiPM, achieved 95±1 ps CTR with 10 mm length crystal elements and 105±2 ps CTR with 20 mm length crystal elements. Compared to the single 10 mm fast crystal side-readout configuration, the proposed side-coupled phoswich design showed worse CTR performance of ~ 9 ps.

The gap materials between 1.9×1.9×10 mm^3 phoswich crystals were also simulated and CTR and LCE results are shown in Figure 6(b). Using an air gap without reflector performed the best in terms of CTR, while using optical grease and reflector showed worse CTR results. Based on these results, we determined the airgap without reflector to be the most efficient proof-of-concept phoswich detector configuration when using fast and slow 1.9×1.9×10 mm^3 crystals side-coupled to a 1-D array of three 4×4 mm^2 SiPMs.

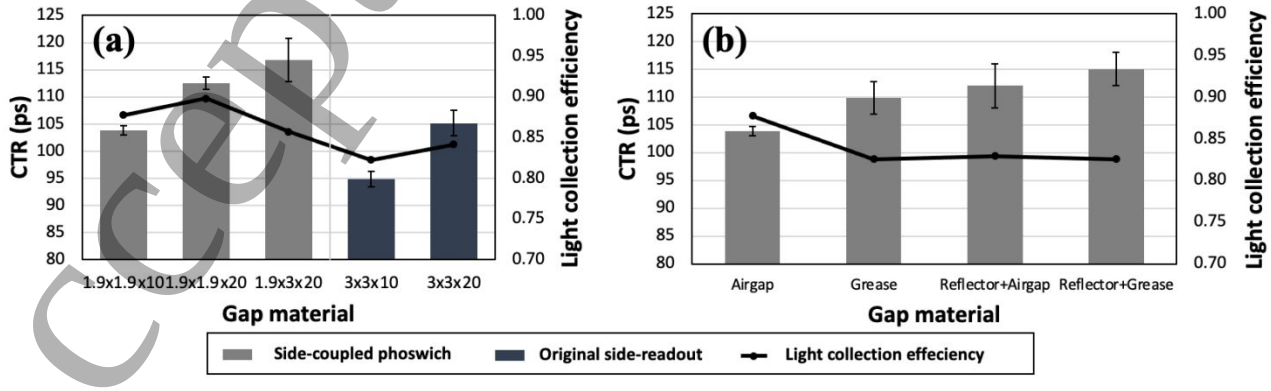

Figure 6 (a) CTR performance of simulated side-readout crystal elements with original single element side-readout configuration and the proposed side-coupled phoswich detector. Each detector configuration was simulated with different crystal cross sectional areas and lengths. The error bar shows the standard deviations over five trials. (b) CTR and LCE performance of the proposed side-coupled phoswich detector when considering different inter-element gap material configurations.

3.2 Experimental results

3.2.1 Crystal characterization

Mean decay times and rise times of two LSO crystals were reported along with standard deviations within eight measurement trials. The decay times were 34.39±0.29 ns and 43.07±0.48 ns and the rise times were 1.74±0.02 ns and 1.93±0.04 ns for fast and slow crystals, respectively. The difference between fast and slow LSO crystal decay times was about 8.68 ns in average. The light ouptut was slightly larger for the fast LSO crystal.

3.2.2 Energy and crystal of interaction separation performance

Figure 7 shows the energy performance of the prototype side-coupled phoswich detector with airgap condition between the crystals. The bias voltage was set to 32 V during acquisition. As shown in Figure 7(a) and Table 2, the fast LSO crystal had a slightly higher light output compared to the slow LSO crystal. The global energy resolution for the side-coupled phoswich detector was 10.5±1.21% in average after SiPM energy non-linearity correction (energy resolution of 9.0±1.02% was observed before the non-linearity correction). Each fast and slow crystal showed an energy resolution of 10.0±0.90% and 9.1±0.52% after the energy non-linearity correction, respectively. Figure 7(b) shows ToT values plotted with the energy values measured from pulse integration; interactions in the two phoswich crystal elements were separable above 200 keV.

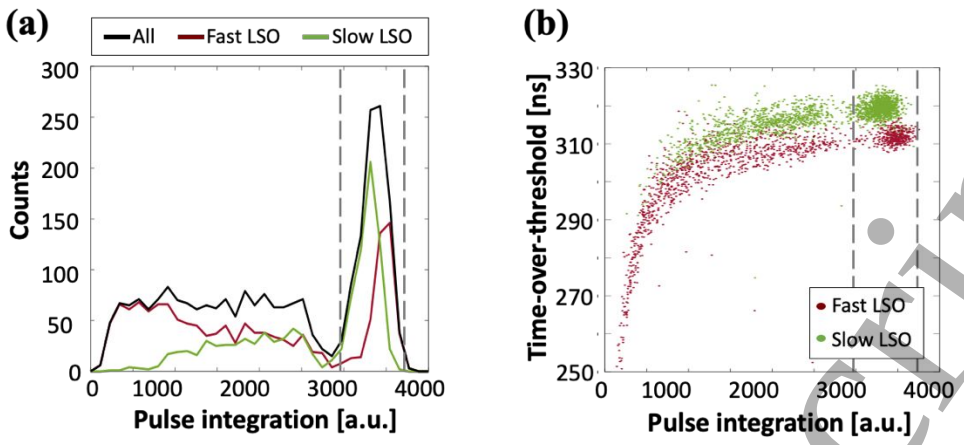

Figure 7 Measurement results of the proof-of-concept side-coupled phoswich detector with an airgap (and no reflector) between the crystal elements (32 V bias voltage). (a) Energy spectra. (b) ToT plotted with the energy calculated based on the pulse integration. The dotted line on the spectra shows the applied energy window.

The crystal-of-interaction separation performance within the phoswich crystals was evaluated based on the ToT histogram (Figure 8(a)). The optimal ToT threshold was selected based on the figure of merit, which was defined as the ratio of the difference of fast and slow crystal separation ($|\mu_{fast} - \mu_{slow}|$) to the sum of the blurring of the two crystal materials ($FWHM_{fast} + FWHM_{slow}$) extracted from a mixture Gaussian model fit to the ToT histogram as shown in Figure 8(b). A ToT threshold of 40% was chosen and Figure 8(a) shows the ToT histogram generated with the events that fell within the FWTM of the 511 keV photopeak. As shown from the ToT histogram, interactions occurring in each of the two crystal elements were clearly resolved showing a crystal-of-interaction separation accuracy of 0.95 at 32V bias voltage. With the reflector between the phoswich crystals, crystal-of-interaction separation accuracy improved to 0.99 with a compromise in energy and coincidence time resolution performance (Table 2). As a comparison, the conventional pulse shape discrimination based on pulse integration showed crystal-of-interaction separation accuracy of 0.87.

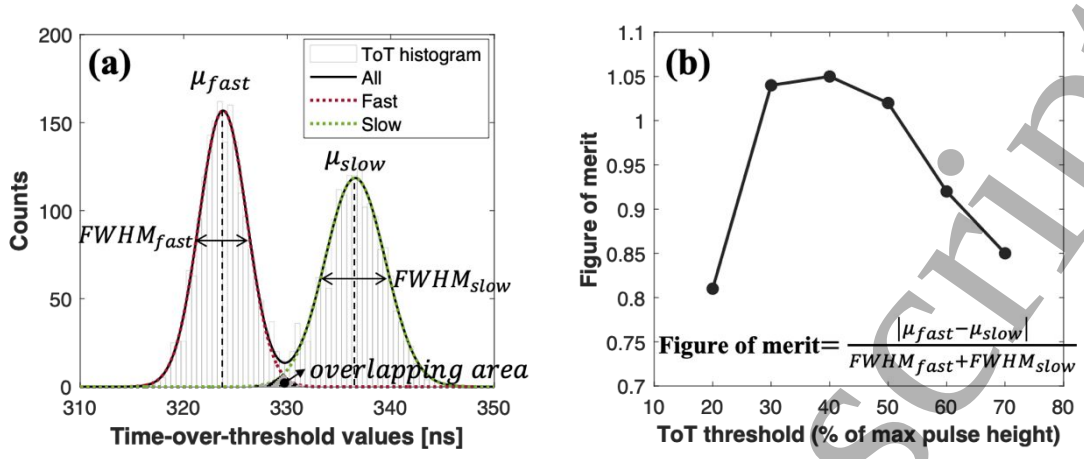

Figure 8 (a) ToT histogram acquired with the ToT threshold of 40% of the maximum pulse height. (b) Figure of merit defined as the ratio of the difference of fast and slow crystal to the sum of their FWHM variances extracted from a mixture Gaussian model fit of the ToT histogram.

Table 2. Detector performances of different detector configurations for side-coupled phoswich detector at 32V bias voltage.

Detector configuration	Fast-Fast	Slow-Slow	Phoswich (airgap)	Phoswich (reflector)
Relative photopeak position	1.000±0.043	0.987±0.036	0.994±0.038	0.910±0.027
Energy resolution (before non-linearity correction)	10.0±0.90% (8.5±0.78%)	9.1±0.52% (7.8±0.45%)	10.5±1.21% (9.0±1.02%)	11.5±1.45% (9.9±1.29%)
Crystal separation accuracy	N/A	N/A	0.95	0.99
CTR	95±1 ps	109±2 ps	107±3 ps	112±4 ps

3.2.3 Coincidence time resolution

Figure 9(a) shows the CTR performance of four different detector combinations at 32 V SiPM bias voltage. For all four combinations, the best CTR was achieved at level of ~2 to 2.2 mV LED thresholds. This LED threshold range is at the level of the first photon above noise and we were able to pick off the timestamp at this low level using a high performance digital oscilloscope and the low-noise high bandwidth amplified pulses. As expected from the simulation as well, the side-coupled phoswich configuration shows worse measured CTR performance compared to the single fast-fast crystal combination and CTR performance was dominated by the slow crystal rise/decay time performance. We also see that using a reflector between the two crystals in the phoswich design degrades CTR performance.

Figure 9(b) shows the best CTR values achieved at each bias voltage with a fixed LED threshold of 2 mV; the error bars, estimated as the standard deviation of the different measurement trials, indicates CTR variances. Better CTR performance was observed at the higher SiPM bias voltages since higher bias leads to higher PDE and gain. For the combinations of fast LSO-fast LSO, slow LSO-slow LSO, and phoswich configuration with airgap (without reflector), and phoswich configuration with reflector, we achieved 95±1 ps, 109±2 ps, 107±3 ps, and 112±4 ps CTR, respectively (Table 2). The time-walk correction was applied for the phoswich configuration because time-walk exists when applying the same LED threshold and the CTR improved, e.g. from 109 ps to 107 ps CTR after the time-walk correction for the phoswich without reflector combination.

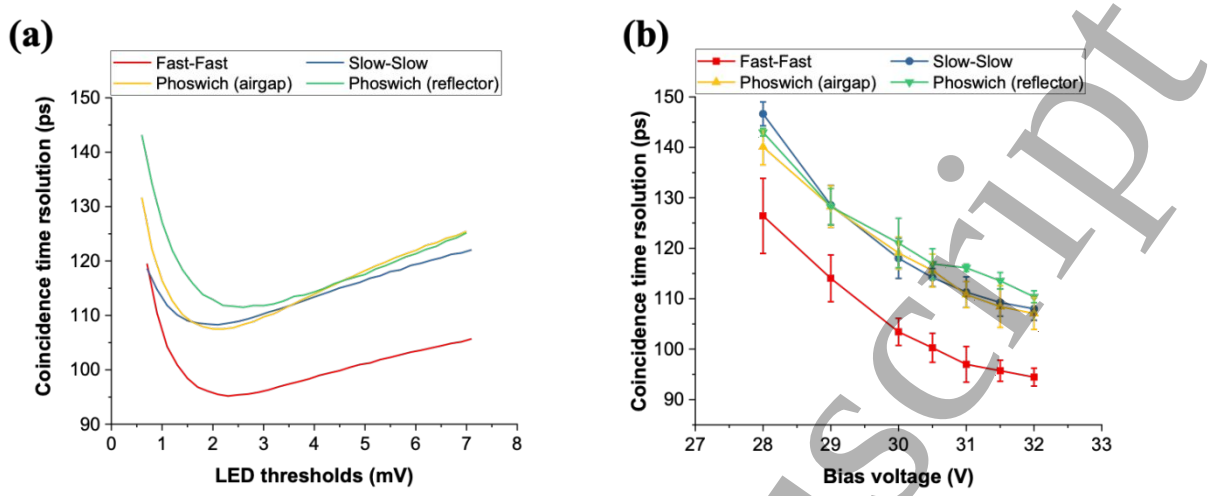

Figure 9 (a) Averaged CTR performance at 32 V SiPM bias voltage as a function of the LED thresholds for different inter-crystal gap material configurations. (b) Averaged CTR values achieved at each SiPM bias voltage with the fixed LED threshold of 2 mV.

4. DISCUSSION

In this study, we proposed a new high-resolution 100-ps TOF PET detector by using a side-by-side phoswich design side-coupled to an array of SiPMs. Based on our simulation study, as shown in Figure 6(a), we optimized the side-coupled phoswich design with 100-ps CTR performance using 1.9×1.9×10 mm^3 crystals side-coupled to a common 1-D array of three 4×4 mm^2 SiPMs. With 20 mm crystal element length, slightly higher LCE but ~ 10ps worse CTR was observed because longer length of crystal increases photon transit time jitter, in addition to the need to use more SiPM pixels in the side-readout configuration. Compared to the original single side-readout configuration with 3×3 mm^2 crystal cross section, the proposed phoswich configuration with 1.9×1.9 mm^2 cross section showed worse CTR even though it had larger LCE, because the phoswich configuration uses larger area SiPM (higher overall capacitance, dark count rate, and uncorrelated and correlated noise rates). Moreover, the phoswich crystal has the secondary boundary (i.e. air) between crystals which will lead to complex optical paths (i.e. photon transport and escape from the crystal is complicated by an interface).

Different gap material between phoswich crystals impacted on the CTR performance. The air gap showed the best CTR results, and when introducing a gap material (e.g. optical grease), worse CTR results were observed due to the LCE drop from 0.88 to 0.83 (Figure 6(b)). Moreover, when a reflector is additionally introduced in between a gap (e.g. airgap or optical grease), we observed further CTR degradation from the simulation results (Figure 6(b)). Using a reflector between crystals generally helps to prevent scintillation light cross-talk and to keep the escaping photons inside the crystal. However, in a side-readout configuration, where a photon transit distance is shorter compared to the end-readout configuration (on average almost five times shorter in this study) which has high LCE, inserting a reflector does not assist in reducing LCE or scintillation photon transit time variance. We hypothesize that the presence of gap materials and reflector leads to more complicated photon paths at the interfaces, which

may trap photons or cause them to escape from the crystal. The experimental results showed less CTR difference in air gap and reflector cases (Figure 9) compared to that of simulation, because in a real situation, the optical grease usually smears into the gap between crystals which worsens the CTR performance.

Moreover, the proposed side-coupled phoswich design uses larger area SiPMs compared to the original single-element side-coupled design (see Figure 1(b)). By using a larger area SiPM, the proposed phoswich design can reduce the total number of SiPM channels that helps to reduce readout complexity while achieving better intrinsic spatial resolution since narrower crystal elements are read out. However, the larger area SiPM has higher parasitic capacitance that affects the rising edge of the scintillation pulse and leads to CTR degradation. We have experimentally measured and compared the CTR performance by conducting the same coincidence measurements with the 3×3 mm^2 SiPM pixel. CTR values of 80±2 ps (Lee *et al* 2019) and 95±3 ps were respectively achieved using a single fast or slow LSO crystal element coupled to 3×3 mm^2 SiPMs; compared to the 4×4 mm^2 SiPM used in this study, about 13 ps CTR degradation is introduced due to the increased SiPM pixel size. An alternative readout method that leverages low noise and high-speed electronics may also remove the parasitic capacitance effects and additionally improve CTR performance (Cates *et al* 2018, Cates and Levin 2019).

In the described detector readout circuit, we propose to use ToT approach for the phoswich crystal-of-interaction separation and the energy measurement. As shown in the results section, the ToT approach showed very good crystal-of-interaction separation, however, as shown in Figure 7(b), there still exists the energy non-linearity issue in case of ToT approach. To improve the ToT energy linearity, alternative methods can be applied (Nishido *et al* 2009, Pourashraf *et al* 2019, Won *et al* 2020).

As mentioned earlier in the introduction, we believe that the proposed side-coupled

phoswich design can be used as a clinically relevant design (effective crystal element length ≥20 mm) with high resolution (<1.9 mm) and 100-ps FWHM CTR performance. By stacking two prototype 10-mm-long phoswich crystals in the radial direction, we can make an effective 20-mm-length crystal element, coupled to 5×1 array of 4×4 mm^2 SiPM array to build a clinically relevant, high resolution, TOF detector design. When scaled-up to an array level of phoswich crystals, each phoswich crystal may require separate ToT electronics leading to complicated front-end electronics. The NINO chip (Anghinolfi *et al* 2004), which is an ultra-fast and low-power front-end amplifier/discriminator AISC, is one potential solution to generate the ToT signal. Moreover, since this NINO chip is also developed for high precision measurement, using NINO chip as an additional timing signal processor combined with a low jitter time-to-digital converter will be a solution to reach a very low LED threshold at the level of few photons in order to promote excellent CTR.

5. SUMMARY AND CONCLUSION

In this study, we propose a novel "side-coupled phoswich" detector configuration for a high resolution clinical TOF-PET system. With the combination of the phoswich scintillation detector concept and a side-readout configuration, we were able to achieve excellent CTR performance of nearly 100-ps FWHM using a phoswich detector configuration comprising side-by-side 1.9×1.9×10 mm^3 crystal elements coupled to the same SiPMs. Moreover, by using the difference in scintillation photon decay time, we can discriminate photon interactions in two phoswich crystal elements without introducing additional sensor channels. The proof-of-concept side-coupled phoswich detector showed energy resolution of 10.5±1.21%, CTR of 107±3 ps, and excellent crystal separation of 95% using two 1.9×1.9×10 mm^3 LSO phoswich crystals in combination with the ToT approach.

6. ACKNOWLEDGMENTS

We thank Matthias Scmand and Maciej Kapusta (Siemens Healthineers) for providing us LSO crystals. This work was supported in part by NIH grants 5R01CA21466903 and 1R01EB02512501.

7. REFERENCES

Abraham A T and Feng J 2011 Evolution of brain imaging instrumentation *Seminars Nucl. Med.* **41** 202–19

Acerbi F and Gundacker S 2019 Understanding and simulating SiPMs *Nucl. Instrum. Methods Phys. Res. A* **926** 16–35

Almeida F G et al 2008 Development of a high packing fraction detector module with DOI measurement capability for high-resolution PET *IEEE Nucl. Sci. Symp. Conf. Record* 3797–800

Anghinolfi F, Jarron P, Martemiyanovb A N, Usenkoc E, Wenningera H, Williamsd M C S and Zichichide A 2004 NINO: an ultra-fast and low-power front-end amplifier/discriminator asic designed for the multigap resistive plate chamber *Nucl. Instrum. Methods Phys. Res. A.* **533** 183–7

Borghi G, Peet B J, Tabacchini V and Schaart D R 2016 A 32 mm× 32 mm× 22 mm monolithic LYSO: Ce detector with dual-sided digital photon counter readout for ultrahigh-performance TOF-PET and TOF-PET/MRI *Phys. Med. Biol.* **61** 4929–49

Cates J W, Vinke R and Levin C S 2015 Analytical calculation of the lower bound on timing resolution for PET scintillation detectors comprising high-aspect-ratio crystal elements *Phys. Med. Biol.* **60** 5141–61

Cates J W and Levin C S 2018 Evaluation of a clinical TOF-PET detector design that achieves 100 ps coincidence time resolution *Phys. Med. Biol.* **63** 115011

Cates J W, Gundacker S, Auffray E, Lecoq P and Levin C S 2018 Improved single photon time resolution for analog SiPMs with front end readout that reduces influence of electronic noise. *Phys. Med. Biol.* **63** 185022

Cates J W and Levin C S 2019 Electronics method to advance the coincidence time resolution with bismuth germinate *Phys. Med. Biol.* **64** 175016

Chang C M, Cates J W and Levin C S 2016 Time-over-threshold for pulse shape discrimination in a time-of-flight phoswich PET detector *Phys. Med. Biol.* **62** 258

Conti M 2011 Why is TOF PET reconstruction a more robust method in the presence of inconsistent data? *Phys. Med. Biol.* **56** 155–68

Conti M and Bendriem B 2019 The new opportunities for high time resolution clinical TOF PET *Clin. Transl. Imaging* **7** 139–47

Gundacker S, Turtos R M, Auffray E, Paganoni M and Lecoq P 2019 High-frequency SiPM readout advances measured coincidence time resolution limits in TOF-PET *Phys. Med. Biol.* **64** 055012

Grant A M and Levin C S 2014 A new dual threshold time-over-threshold circuit for fast timing in PET *Phys. Med. Biol.* **59** 3421

Holte S, Ostertag H and Kesselberg M 1987 A preliminary evaluation of a dual crystal positron camera. *J. Comput. Assisted Tomography* **11** 691–7

Hsu D F C, Ilan E, Peterson W T, Uribe J, Lubberink M and Levin C S 2017 Studies of a next-generation silicon-photomultiplier–based time-of-flight PET/CT system *J. Nucl. Med.* **58** 1511–18

Inadama N, Murayama H, Yamaya T, Kitamura K, Yamashita T, Kawai H, Tsuda T, Sato M, Ono Y and Hamamoto M 2006 Preliminary evaluation of four-layer BGO DOI-detector for PET *IEEE Trans. Nucl. Sci.* **53** 30–4

Ito M, Lee M S and Lee J S 2013 Continuous depth-of-interaction measurement in a single-layer pixelated crystal array using a single-ended readout *Phys. Med. Biol.* **58** 1269–82

Jakoby B W, Bercier Y, Conti M, Casey M E, Bendriem B and Townsend D W 2011 Physical and clinical performance of the mCT time-of-flight PET/CT scanner *Phys. Med. Biol.* **56** 2375–89

Jan S *et al* 2004 GATE: a simulation toolkit for PET and SPECT *Phys. Med. Biol.* **49** 4543–

61

Janecek M and Moses W W 2010 Simulating scintillator light collection using measured optical reflectance *IEEE Trans. Nucl. Sci.* **57** 964–70

Jan S *et al* 2011 GATE V6: a major enhancement of the GATE simulation platform enabling modelling of CT and radiotherapy *Phys. Med. Biol.* **56** 881–901

Kang HG, Yamaya T, Han YB, Song SH, Ko GB, Lee JS and Hong SJ 2020 Crystal surface and reflector optimization for the SiPM-based dual-ended readout TOF-DOI PET detector *Biomed. Phys. Eng. Express* **6** 065028

La Bella A, Tavernier S, Woody C, Purschke M, Zhao W and Goldan AH 2020 Towards 100 ps coincidence time resolution using multiple timestamps in depth-encoding PET modules: a Monte Carlo simulation study *IEEE Trans. Rad. Plasma Med. Sci.* **in press:** https://doi.org/10.1109/TRPMS.2020.3043691

Lee M S, Cates J W, Kapusta M, Schmand M and Levin C S 2019 Study of Lutetium-based scintillators for PET system design with 100-ps coincidence time resolution *IEEE Nucl. Sci. Symp. Med. Imaging Conf.* doi: 10.1109/NSS/MIC42101.2019.9059972

Lecoq P 2017 Pushing the Limits in Time-of-Flight PET Imaging *IEEE. Trans. Rad. Plasma. Med. Sci.* **1** 473–85

Levin A and Moisan C 1996 A more physical approach to model the surface treatment of scintillation counters and its implementation into DETECT *IEEE Nucl. Sci. Symp. Conf. Rec.* **2** 702–6

Levin C S 2002 Design of a high-resolution and high-sensitivity scintillation crystal array for PET with nearly complete light collection *IEEE Trans. Nucl. Sci.* **49** 2236–43

Loignon-Houle F, Toussaint M, Lee M S, Cates J W and Lecomte R 2020 Experimental validation of a coincidence time resolution metric including depth-of-interaction bias for TOF-PET *Phys. Med. Biol.* **65** 245004

LSO(Ce) Lutetium Oxyorthosilicate (Ce) ΣTech[UK] **datasheet**: https://www.advatech-uk.co.uk/lso_ce.html

Miller M, Zhang J, Binzel K, Griesmer J, Laurence T, Narayanan M, Natarajamani D, Wang S and Knopp M 2015 Characterization of the Vereos digital photon counting PET system *J. Nucl. Med.* **56** 434

Miyaoka R S, Li X, Lockhart C and Lewellen T K 2009 New continuous miniature crystal element (cMiCE) detector geometries *IEEE Nucl. Sci. Symp. Med. Imaging Conf.* pp 3639–42

Mollet P, Keereman V, Clementel E and Vandenberghe S 2012 Simultaneous MR-compatible emission and transmission imaging for PET using time-of-flight information *IEEE Trans. Med. Imaging* **31** 1734–42

Nemallapudi M V, Gundacker S, Lecoq P and Auffray E 2016 Single photon time resolution of state of the art SiPMs *J. Instr.* **11** P10016

Nishino H *et al* 2009 High-speed charge-to-time converter ASIC for the Super-Kamiokande detector *Nucl. Instrum. Methods Phys. Res. A* **610** 710–7.

ON Seminconductor 2018 Silicon Photomultipliers (SiPM), High PDE and Timing Resolution Sensors in a TSV Package Datasheet: *https://www.onsemi.com/pub/Collateral/MICROJ-SERIES-D.PDF*

Pizzichemi M, Polesell A, Stringhini G, Gundacker S, Lecoq P, Tavernier S, Paganoni M and AuffrayE 2019 On light sharing TOF-PET modules with depth of interaction and 157 ps FWHM coincidence time resolution *Phys. Med. Biol.* **64** 155008

Pourashraf S, Cates J W, Lee M S and Levin C S 2019 Pulse Shape Discrimination and Energy Measurement in Phoswich Detectors Using Gated-Integrator Circuit *IEEE Nucl. Sci. Symp. Med. Imaging Conf.* doi: 10.1109/NSS/MIC42101.2019.9059824

Regazzoni V, Acerbi F, Cozzi G, Ferri A, Fiorini C, Paternoster G, Piemonte C, Rucatti D, Zappala G, Zorzi N and Gola A 2017 Characterization of high density SiPM non-linearity and

energy resolution for prompt gamma imaging applications *J. Instr.* **12** P07001

Shao Y, Meadors K, Silverman R W, Farrell R, Cirignano L, Grazioso R, Shah K S and Cherry S R 2002 Dual APD array readout of LSO crystals: optimization of crystal surface treatment *IEEE Trans. Nucl. Sci.* **49** 649–54

Siemens Biograph Vision Technical Sheet, retrieved April 2019 www.siemens-healthineers.com

Sluis J, de Jong J, Schaar J, Noordzij W, van Snick P, Dierckx R, Borra R, Willemsen A and Boellaard R 2019 Performance Characteristics of the Digital Biograph Vision PET/CT System *J. Nucl. Med.* **60** 1031–36

Surti S 2015 Update on time-of-flight PET imaging *J Nucl. Med.* **56** 98–105

Surti S, Karp J S 2016 Advances in time-of-flight PET *Physica Medica* **32** 12–22

Watanabe M, Saito A, Isobe T, Ote K, Yamada R, Moriya T and Omura T 2017 Performance evaluation of a high-resolution brain PET scanner using four-layer MPPC DOI *Phys. Med. Biol.* **62** 7148

Tashima H and Yamaya T 2016 Proposed helmet PET geometries with add-on detectors for high sensitivity brain imaging *Phys. Med. Biol*. **61** 7205

Van der Laan D J J, Schaart D R, Maas M C, Beekman F J, Bruyndonckx P and van Eijk E 2010 Optical simulation of monolithic scintillator detectors using GATE/GEANT4 *Phys. Med. Biol.* **55** 1659–75

Won J Y and Lee J S 2018 Highly Integrated FPGA-Only Signal Digitization Method Using Single-Ended Memory Interface Input Receivers for Time-of-Flight PET Detectors *IEEE Trans. Biomed. Circuits Syst.* **12** 1401–9

Won J Y, Ko G B, Kim K Y, Park H, Lee S, Son J W and Lee J S 2020 Comparator-less PET data acquisition system using single-ended memory interface input receivers of FPGA *Phys. Med. Biol.* **65** 155007

Yamaya T, Yoshida E, Obi T, Ito H, Yoshikawa K and Murayama H 2008 First human brain imaging by the jPET-D4 prototype with a pre-computed system matrix *IEEE Trans. Nucl. Sci.* **55** 2482–92

Yeom J Y, Vinke R and Levin C S 2014 Side readout of long scintillation crystal elements with digital SiPM for TOF-DOI PET *Med. Phys.* **41** 122501